

A Direct Sampling Method for Inverse Electromagnetic Medium Scattering

Kazufumi Ito* Bangti Jin† Jun Zou‡

November 11, 2018

Abstract

In this paper, we study the inverse electromagnetic medium scattering problem of estimating the support and shape of medium scatterers from scattered electric or magnetic near-field data. We shall develop a novel direct sampling method based on an analysis of electromagnetic scattering and the behavior of the fundamental solution. The method is applicable even with one incident field and needs only to compute inner products of the measured scattered field with the fundamental solutions located at sampling points. Hence it is strictly direct, computationally very efficient, and highly tolerant to the presence of noise in the data. Two- and three-dimensional numerical experiments indicate that it can provide reliable support estimates of one single and multiple scatterers in case of both exact and highly noisy data.

Key Words: inverse medium scattering, direct sampling method, scattering analysis, electromagnetic wave propagation

1 Introduction

Inverse electromagnetic scattering represents an important noninvasive imaging technology for interrogating material properties, and it arises in many practical applications such as biomedical diagnosis [28, 6], nondestructive testing [9], and geophysical exploration [12]. In this work we are concerned with the inverse medium problem of determining the electrical/magnetic properties of unknown inhomogeneous objects embedded in a homogeneous background from noisy measurements of the scattered electric/magnetic field corresponding to one or several incident fields impinged on the objects. Mathematically, the medium scattering problem is described by the time-harmonic Maxwell system:

$$\begin{aligned} i\omega\epsilon E + \nabla \times H &= 0 & \text{in } \mathbb{R}^d, \\ -i\omega\mu H + \nabla \times E &= 0 & \text{in } \mathbb{R}^d, \end{aligned}$$

where the vectorial fields H and E denote the magnetic and electric fields, respectively. Here the constant ω is the angular frequency, the functions ϵ and μ refer to the electrical permittivity and magnetic permeability, respectively.

Let the domain $\Omega \subset \mathbb{R}^d$ ($d = 2, 3$) be the space occupied by the inhomogeneous medium objects within the homogeneous background \mathbb{R}^d . We are interested in either electrical or magnetic inhomogeneities, but shall focus our discussions on the case of electrical inhomogeneities since the case of magnetic inhomogeneities follows analogously. So we shall assume $\mu = \mu_0$, i.e., the magnetic permeability of the

*Department of Mathematics and Center for Research in Scientific Computation, North Carolina State University, Raleigh, North Carolina (kito@unity.ncsu.edu).

†Department of Mathematics and Institute for Applied Mathematics and Computational Science, Texas A&M University, College Station, Texas 77843-3368, USA (btjin@math.tamu.edu).

‡Department of Mathematics, Chinese University of Hong Kong, Shatin, N.T., Hong Kong (zou@math.cuhk.edu.hk).

background. Then by taking the curl of the second equation of the system and eliminating H in the first equation, we obtain the following vector Helmholtz equation for the electric field E

$$\nabla \times (\nabla \times E) - k^2 n^2(x) E = 0 \quad (1)$$

where k is the wavenumber, with $k^2 = \omega^2 \epsilon_0 \mu_0$, and $n = \frac{1/\sqrt{\epsilon_0 \mu_0}}{1/\sqrt{\epsilon \mu_0}}$ is the refractive index function, i.e., the ratio of the wave velocity in the homogeneous background medium to that in the inhomogeneities. The refractive index n completely characterizes the electrical inhomogeneities, and the support is filled by the inhomogeneous media, i.e., $\text{supp}(n^2 - 1) = \Omega$. Further, we assume that the medium scattering is excited by an incident plane wave E^i :

$$E^i = p e^{ikd \cdot x},$$

where $d \in \mathbb{S}^{d-1}$ and $p \in \mathbb{S}^{d-1}$ are the incident and polarization directions, respectively. Since the incident field E^i is solenoidal, i.e., $\nabla \cdot E^i = 0$, the polarization p should be chosen such that it is perpendicular to the incident direction d . Then the incident field E^i satisfies the Maxwell system (1) in the entire homogeneous background. The forward scattering problem is to find the total electric field E given the refractive index n^2 , under the following Silver-Müller radiation condition for the scattered field $E^s = E - E^i$:

$$\lim_{|x| \rightarrow \infty} |x|^{\frac{d-1}{2}} (\nabla \times E^s \times \hat{x} - ikE^s) = 0$$

uniformly for all directions $\hat{x} = x/|x| \in \mathbb{S}^{d-1}$.

The inverse problem of our interest is the inverse medium scattering problem, which is to reconstruct the inhomogeneous media from the scattered electric field E^s corresponding to one (or several) incident field E^i , measured over a certain closed curve/surface Γ . In view of the practical significance of the inverse problem, there has been considerable interest in designing efficient and stable inversion techniques. However, this is very challenging because of a number of complicating factors: strong nonlinearity of the map from the refractive index to the scattered field, severe ill-posedness of the inverse problem, complexity of the forward model, and the limited available and noisy data. Nonetheless, a number of imaging algorithms have been developed in the literature, which can be roughly divided into two categories: direct and indirect methods. The former aims at detecting the scatterer support and shape, and includes linear sampling method (LSM) [10, 7], multiple signal classification (MUSIC) [14], and asymptotic analysis [3]. In contrast, the latter provides a distributed estimate of the refractive index by applying regularization techniques. We refer interested readers to the adjoint-based method [15, 30, 22], the recursive linearization (with continuation in frequency) [4, 5], the Gauss-Newton method [18, 13, 19], the contrasted source inversion [2], subspace regularization [8] and level set method [16] for an incomplete list. Generally, the estimates by the method of the latter category can provide more details of the inclusions/inhomogeneities, but at the expense of much increased computational efforts, especially when the forward model is the full Maxwell system.

In this work, we shall develop a novel direct method, called the direct sampling method, for stably and accurately detecting the support of the scatterers. These sampling-type methods are direct in the sense that no optimizations or solutions of linear systems are involved, so they are computationally very cheap. They have attracted some attentions in very recent years; see [26] and [21] for inverse acoustic scattering problems using far-field data and near-field data, respectively. A different derivation of the method due to Potthast [26] was given in [24], where the performance of the methods using near-field and far-field data was compared in detail and the effectiveness of these methods was also investigated for several important scattering scenarios: obstacles, inhomogeneous media, cracks and their combinations.

The major goal of this work is to extend the direct sampling method developed in [21] for the acoustic scattering to the electromagnetic scattering. Due to the much increased complexity of the Maxwell's system relative to its scalar counterpart, the Helmholtz equation, the extension is nontrivial and requires several innovations. It is based on an integral representation of the scattered field, a careful analysis on electromagnetic scattering and the behavior of the fundamental solutions. Numerically, it involves only computing inner products of the measured scattered field E^s with fundamental solutions to the Maxwell system located at sampling points over the measurement surface Γ . Hence it is strictly direct and does

not use any matrix operations or minimizations, and its implementation is very straightforward. Our extensive numerical experiments indicate that it can provide an accurate and reliable estimate of the scatterer support, even in the presence of a fairly large amount of noises in the data. Hence, it represents an effective yet simple computational tool for reliably detecting the scatterer support. In practice, a rough estimate of the scatterer support may be sufficient for many purposes [29]. And if desired, one can obtain a more refined estimate of the medium scatterers by, e.g., any aforementioned indirect imaging methods or the one from [20], using the estimate from the direct sampling method to provide an initial computational domain, which is usually much smaller than the originally selected sampling domain. Since indirect imaging methods often involve highly nonlinear optimization processes, an accurate and smaller initial domain can essentially reduce the entire computational efforts.

The direct sampling method developed below uses a sampling strategy, and its flavor closely resembles MUSIC and the LSM (see [25, 7] for overviews). However, it differs significantly from these two techniques. Firstly, it works with a few incident fields, whereas the latter two require the full map (multi-static response matrix/far-field operator) or data from sufficiently many incidents. Secondly, our method does not perform any matrix operations, e.g. eigendecomposition in MUSIC or solving ill-posed integral equations in the LSM. Hence, our method is computationally efficient. Lastly, the noise is treated directly via the inner product, which automatically filters out the noise contribution, and thus the method is highly tolerant to noises.

The rest of the paper is organized as follows. In Section 2, we recall an integral reformulation of the Maxwell system, cf. (1), recently derived in [23], which plays an essential role in the derivation of the direct sampling method. Then we develop the method in Section 3 in detail, where a preliminary analysis of its theoretical performance is also provided. In Section 4, we provide two- and three-dimensional numerical experiments to illustrate its distinct features, i.e., accuracy and robustness, for both exact and noisy data. Technical details of the implementation are provided in the appendix.

2 Integral representation of Maxwell System

In this part, we recall an equivalent formulation of the Maxwell system (1), which is fundamental to the derivation of the direct sampling method. We begin with the definition of the fundamental solution $G(x, y)$ to the scalar Helmholtz equation, i.e.,

$$(-\Delta - k^2)G(x, y) = \delta(x - y)$$

where $\delta(x - y)$ is the Dirac delta function with the singularity located at $y \in \mathbb{R}^d$. We know that $G(x, y)$ has the following representations (see, e.g., [11])

$$G(x, y) = \begin{cases} \frac{i}{4} H_0^{(1)}(k|x - y|), & d = 2; \\ \frac{1}{4\pi} \frac{e^{ik|x - y|}}{|x - y|}, & d = 3, \end{cases}$$

where the function $H_0^{(1)}$ refers to Hankel's function of the first kind and zeroth order. Using the scalar function $G(x, y)$ we can define a matrix-valued function $\Phi(x, y)$ by

$$\Phi(x, y) = k^2 G(x, y) I + D^2 G(x, y) \quad (2)$$

where $I \in \mathbb{R}^{d \times d}$ is the identity matrix and D^2 denotes the Hessian of G . Then we can verify by some direct calculations that $\nabla \cdot \Phi(x, y) = 0$ and

$$\nabla \times \nabla \times \Phi(x, y) - k^2 \Phi(x, y) = \delta(x - y) I, \quad (3)$$

where (and in the sequel) the actions of the operators $\nabla \cdot$ and $\nabla \times$ on a matrix-valued function are always understood to be operated columnwise. Hence, the matrix $\Phi(x, y)$ defined by (2) is a divergence-free

fundamental solution to the Maxwell system (1) in the homogeneous space \mathbb{R}^d . Using the fundamental solution $\Phi(x, y)$, the total electric field $E(x)$ can be represented by the following integral equation

$$E(x) = E^i + \int_{\mathbb{R}^d} \Phi(x, y)(n^2 - 1)E(y)dy. \quad (4)$$

We note that the fundamental solution $\Phi(x, y)$ involves a non-integrable singularity at $x = y$. Hence care must be exerted when interpreting the integral, in the case that the point x lies within the domain Ω [17]. Next we let $\eta = n^2 - 1$, which precisely profiles the inhomogeneities of the media. In particular, the support of η coincides with the scatterer support Ω . Furthermore, we introduce the function $J = (n^2 - 1)E$, that is the induced electrical current caused by the medium inhomogeneities. Then, the total electric field $E(x)$ satisfies [11, Theorem 9.1]

$$E(x) = E^i(x) + k^2 \int_{\mathbb{R}^d} G(x, y)J(y) dy + \nabla_x \int_{\mathbb{R}^d} G(x, y)\text{div}_y J(y) dy.$$

Upon noting the reciprocity relation $\nabla_x G(x, y) = -\nabla_y G(x, y)$ and applying integration by parts to the second integral term on the right hand side, we arrive at the following equivalent integral equation

$$E(x) - \int_{\mathbb{R}^d} G(x, y)PJ(y) dy = E^i(x)$$

where the operator P is defined by

$$P\phi = k^2 I\phi + \text{grad}(\text{div}\phi).$$

Thus, by multiplying the equation with the coefficient η , we obtain an integral equation for the generalized electric current J

$$J(x) - \eta \int_{\Omega} G(x, y)PJ(y) dy = \eta E^i(x), \quad x \in \Omega. \quad (5)$$

The above equation was rigorously justified in suitable function spaces in [23], and it is very convenient for solving inverse problems; see [23] for the inverse source problem and [22] for inverse medium scattering. Compared with the whole-space Maxwell system, the integral equation (5) is defined over the scatterer support Ω since the induced current J vanishes identically outside the scatterer support $\Omega = \text{supp}(\eta)$. This reduces greatly the computational domain, and hence brings significant computational convenience. We shall adopt the integral equation (5) for the forward scattering simulation, which can be discretized numerically by the mid-point quadrature rule (cf. Appendix A for details).

3 Direct sampling method

In this section, we develop a novel direct sampling method to determine the locations, the number and the shape of the scatterers/inhomogeneities in electromagnetic wave propagation. It is based on an analysis for electromagnetic scattering. Methodologically, it extends our earlier work on the acoustic scattering [21]. We shall also provide an analysis of the theoretical performance of the method by examining the behaviors of the fundamental solution. For the sake of convenience, we introduce the domain Ω_Γ , which is the domain enclosed by the circular/spherical measurement surface Γ , and use (\cdot, \cdot) for the real inner product on \mathbb{C}^d and the overbar for the complex conjugate.

3.1 Direct sampling method

In this part, we develop a novel direct sampling method (DSM). The derivation relies essentially on the following two basic facts. The first is the representation of the scattered electric field E^s using the fundamental solution Φ by (cf. (4)):

$$E^s(x) = \int_{\Omega} \Phi(x, y)J(y)dy \quad \forall x \in \Gamma. \quad (6)$$

The second fact is an important relation for the fundamental solution $\Phi(x, y)$ (2) to the Maxwell system (1). For any two arbitrary sampling points x_p and x_q which lie inside domain Ω_Γ but are away from its boundary Γ , we have the following approximation

$$\int_{\Gamma} (\Phi(x, x_p)p, \bar{\Phi}(x, x_q)q) ds \approx k^{-1} \Im(p, \Phi(x_p, x_q)q) \quad \forall p, q \in \mathbb{R}^d. \quad (7)$$

Next, we derive this crucial correlation. To do so, we first show the following lemma.

Lemma 3.1. *Let x_p and x_q be two distinct points lying inside the domain Ω_Γ . Then for any constant vectors $p \in \mathbb{C}^d$ and $q \in \mathbb{R}^d$, there holds that*

$$\int_{\Gamma} (\nabla \times \bar{\Phi}(x, x_q)q \times n, \Phi(x, x_p)p) - (\nabla \times \Phi(x, x_p)p \times n, \bar{\Phi}(x, x_q)q) ds = -2i(p, \Im(\Phi(x_p, x_q)q)). \quad (8)$$

Proof. It is easy to verify directly that the identify $(\nabla \times \nabla \times \Phi(x, x_p))p = \nabla \times \nabla \times \Phi(x, x_p)p$ holds for any constant vector $p \in \mathbb{R}^d$. Using this identify and (3) we have

$$\nabla \times \nabla \times \Phi(x, x_p)p - k^2\Phi(x, x_p)p = \delta(x - x_p)p \quad \forall p \in \mathbb{R}^d, \quad (9)$$

$$\nabla \times \nabla \times \Phi(x, x_q)q - k^2\Phi(x, x_q)q = \delta(x - x_q)q \quad \forall q \in \mathbb{R}^d. \quad (10)$$

Taking the conjugate of equation (10) yields

$$\nabla \times \nabla \times \bar{\Phi}(x, x_q)q - k^2\bar{\Phi}(x, x_q)q = \delta(x - x_q)q. \quad (11)$$

By taking (real) inner products of equation (9) with $\bar{\Phi}(x, x_q)q$ and of equation (11) with $\Phi(x, x_p)p$, then subtracting the two identities, we arrive at

$$\begin{aligned} \int_{\Omega_\Gamma} \{(\bar{\Phi}(x, x_q)q, \nabla \times \nabla \times \Phi(x, x_p)p) - (\Phi(x, x_p)p, \nabla \times \nabla \times \bar{\Phi}(x, x_q)q)\} dx \\ = (p, \bar{\Phi}(x_p, x_q)q) - (q, \Phi(x_p, x_q)p). \end{aligned} \quad (12)$$

Next we apply the following integration by parts formula

$$\begin{aligned} \int_{\Omega_\Gamma} \{(\bar{\Phi}(x, x_q)q, \nabla \times \nabla \times \Phi(x, x_p)p) - (\Phi(x, x_p)p, \nabla \times \nabla \times \bar{\Phi}(x, x_q)q)\} dx \\ = \int_{\Gamma} (\nabla \times \bar{\Phi}(x, x_q)q \times n, \Phi(x, x_p)p) - (\nabla \times \Phi(x, x_p)p \times n, \bar{\Phi}(x, x_q)q) ds \end{aligned}$$

to the left hand side of (12) to obtain

$$\begin{aligned} \int_{\Gamma} (\nabla \times \bar{\Phi}(x, x_q)q \times n, \Phi(x, x_p)p) - (\nabla \times \Phi(x, x_p)p \times n, \bar{\Phi}(x, x_q)q) ds \\ = (p, \bar{\Phi}(x_p, x_q)q) - (q, \Phi(x_p, x_q)p). \end{aligned}$$

Now the real symmetry of the fundamental solution $\Phi(x, y)$ leads directly to the identify (8). \square

Next, note that on a circular curve/spherical surface Γ , we can approximate the left hand side of identity (8) by means of the Silver-Müller radiation condition for the outgoing fundamental solution $\Phi(x, y)$ to the Maxwell system, i.e.,

$$\nabla \times \Phi(x, x_p)p \times n = ik\Phi(x, x_p)p + \text{h.o.t.}$$

Thus we have the following approximations:

$$\begin{aligned} \nabla \times \Phi(x, x_p)p \times n &\approx ik\Phi(x, x_p)p, \\ \nabla \times \bar{\Phi}(x, x_q)q \times n &\approx -ik\bar{\Phi}(x, x_q)q, \end{aligned}$$

which are valid if the points x_p and x_q are not close to the boundary Γ . Consequently, we arrive at the following important approximate relation:

$$- \int_{\Gamma} \left\{ (ik \Phi(x, x_p)p, \bar{\Phi}(x, x_q)q) + (ik \bar{\Phi}(x, x_q)q, \Phi(x, x_p)p) \right\} ds \approx -2i(p, \Im(\Phi(x_p, x_q))q).$$

Upon simplifying the relation, we arrived at the desired relation (7).

The relation (7) leads us to a very important observation: the following integral over the measurement surface Γ

$$\langle \Phi(\cdot, x_p)p, \Phi(\cdot, x_q)q \rangle_{L^2(\Gamma)} = \int_{\Gamma} (\Phi(x, x_p)p, \bar{\Phi}(x, x_q)q) ds \quad (13)$$

has a maximum if $x_p = x_q$ and decays to 0 as $|x_p - x_q|$ tends to ∞ , in view of the decay property of the fundamental solution $\Phi(x, y)$.

These two basic facts (6) and (7) are crucial to the derivation of our direct sampling method. Next we consider a sampling domain $\tilde{\Omega} \subset \Omega_{\Gamma}$ that contains the scatterer support Ω , and divide it into a set of small elements $\{\tau_j\}$. Then by using the rectangular quadrature rule, we arrive at the following discrete sum representation

$$E^s(x) = \int_{\tilde{\Omega}} \Phi(x, y)J(y)dy \approx \sum_j \Phi(x, y_j)J(y_j)|\tau_j|, \quad (14)$$

where the point y_j lies within the j th element τ_j , and $|\tau_j|$ denotes the volume/area of the element τ_j . Noting the fact that the generalized induced current J vanishes identically outside the support Ω , the summation in (14) is actually only over those elements that intersect with Ω . We point out that, in practice, the scatterer support Ω may consist of several disjoint subregions, each being occupied by a (possibly different) physical medium. By elliptic regularity theory [11, 31], the induced current $J = \eta E$ is smooth in each subregion, and thus according to classical approximation theory, the approximation in (14) can be made arbitrarily accurate by refining the elements $\{\tau_j\}$. Nonetheless, we reiterate that the relation (14) serves only the goal of motivating our method, and it is not needed in the implementation of our method. Physically, the relation (14) can be interpreted as follows: the scattered electric field E^s at any fixed point $x \in \Gamma$ is a weighted average of that due to the point scatterers located at $\{y_j\}$ lying within the true scatterer Ω .

The approximate relations (7) and (14) together give that for any sampling point $x_p \in \tilde{\Omega}$ and any constant vector $q \in \mathbb{R}^d$, there holds

$$\begin{aligned} \langle E^s, \Phi(\cdot, x_p)q \rangle_{L^2(\Gamma)} &\approx \left\langle \sum_j \Phi(\cdot, y_j)J(y_j)|\tau_j|, \Phi(\cdot, x_p)q \right\rangle_{L^2(\Gamma)} \\ &= \sum_j |\tau_j| \langle \Phi(\cdot, y_j)J(y_j), \Phi(\cdot, x_p)q \rangle_{L^2(\Gamma)} \\ &\approx k^{-1} \sum_j |\tau_j| (J(y_j), \Im(\Phi(x_p, y_j))q). \end{aligned} \quad (15)$$

Due to the behavior of the fundamental solution (see the discussions in Section 3.2), the approximation (15) indicates that the inner product $\langle E^s, \Phi(\cdot, x_p)q \rangle$ may take significant values if the sampling point x_p is close to some physical point scatterer y_j and small values otherwise, thereby acting as an indicator function to the presence of scatterers and equivalently providing an estimate of the scatterer support Ω . In summary, these observations lead us to the following index function:

$$\Psi(x_p; q) = \frac{|\langle E^s, \Phi(\cdot, x_p)q \rangle_{L^2(\Gamma)}|}{\|E^s\|_{L^2(\Gamma)} \|\Phi(\cdot, x_p)q\|_{L^2(\Gamma)}}, \quad \forall x_p \in \tilde{\Omega}. \quad (16)$$

Here $\Phi(\cdot, x_p)q$ acts as a probe/detector for the scatterers. In principle, the choice of the polarization vector q in the index $\Psi(x_p; q)$ can be quite arbitrary. Naturally, it is expected that the choice of q will

affect the capability of the function $\Phi(x, x_p)q$ for probing scatterers. The analysis in Section 3.2 will shed insights into the probing mechanism and will provide useful guidelines for the choice of q . Our experimental experiences indicate that the choice $q = p$, i.e., the polarization of the incident field E^i , works very well in practice. We note that, apart from providing an estimate of the scatterer support, the index $\Psi(x_p; q)$ provides a likelihood distribution of the inhomogeneities in $\tilde{\Omega}$, which up to a multiplicative constant may be used as the an initial estimate of the distributed coefficient η [20].

The DSM is one sampling type imaging technique. There are several existing sampling techniques, e.g., MUSIC and the LSM. The DSM differs from these techniques in several aspects. First, the DSM involves computing only inner products of the measured scattered field with the probing functions $\Phi(x, x_p)q$, i.e., the fundamental solutions with singularity concentrated at sampling points. Therefore, it does not involve any expensive linear algebraic operations, like solving first-kind ill-posed integral equations in the LSM and eigenvalue decomposition for computing the signal space (noise space) in the MUSIC. Secondly, the DSM is applicable to a few (e.g., one or two) incident fields, whereas the LSM requires the far field map and the MUSIC requires the multi-statistic matrix, which necessitates multiple measurements. Therefore, the DSM is particularly attractive in the case of a few scattered data. Thirdly, the DSM treats noise directly via the inner product. The noise roughly distributes the energy in all frequencies equally, whereas the fundamental solutions are smooth with their energy concentrated on low frequency modes. Therefore, the high-frequency modes in the noise are roughly orthogonal to the (smooth) fundamental solutions. In other words, the presence of noise does not cause much changes in the inner product, but the normalization. As a consequence, the DSM is highly tolerant to data noise.

3.2 Analysis of the index function Ψ

In this part, we analyze the theoretical performance and the mechanism of the DSM by analytically and numerically studying the fundamental solution $\Phi(x, y)$ in (2) and the index Ψ in (16) for one single point scatterer. First, we recall the crucial role of the approximate relation (7): the fundamental solution $\Phi(x_p, x_q)$ is nearly singular, and assumes very large values for x_p close to x_q . More precisely, the extremal property of $\Im(\Phi(x_p, x_q))$ paves the way for accurate support detection. This observation is evident for the scalar Helmholtz equation in view of the identity $\Im(G(x_p, x_q)) = \frac{1}{4}J_0(k|x_p - x_q|)$ (in two-dimension), where J_0 is the Bessel function of the first kind of order zero. However, for the Maxwell system, the fundamental solution $\Phi(x, y)$ contains 4 or 9 different entries, and each term exhibits drastically different behavior. So with each different polarization vector q , the probing function $\Phi(x, x_p)q$, as well as the index function $\Psi(x_p; q)$ in (16), mixes different components together and may yield quite different behaviors. Next we shall investigate more closely the properties of $\Phi(x, y)$ in order to have a better understanding and interpretation of the index function $\Psi(x_p; q)$ in (16).

We begin with an important observation on the trace of the fundamental solution $\Phi(x, y)$.

Proposition 3.1. *For $d = 2, 3$, the fundamental solution $\Phi(x, y)$ satisfies the following relation*

$$\text{tr}\Phi(x, y) = (d - 1)k^2G(x, y). \quad (17)$$

Proof. Let us begin with the two-dimensional case, i.e., transverse electric mode, i.e., $E = (E_1, E_2, 0)$ and $H = (0, 0, H_3)$. Then the Maxwell system (1) should be understood as

$$\begin{aligned} i\omega\mu_0 H_3 &= (\nabla \times E)_3 = \frac{\partial E_2}{\partial x_1} - \frac{\partial E_1}{\partial x_2} \\ -i\omega\epsilon E &= \nabla \times H = \left(\frac{\partial H_3}{\partial x_2}, -\frac{\partial H_3}{\partial x_1} \right). \end{aligned}$$

The fundamental solution $G(x, y)$ is given by $G(x, y) = \frac{i}{4}H_0^{(1)}(k|x - y|)$. To evaluate the Hessian $D^2G(x, y)$, we first recall the recursive relation for the derivative of Hankel functions [1]

$$\frac{d}{dz}H_n^{(1)}(z) = \frac{nH_n^{(1)}(z)}{z} - H_{n+1}^{(1)}(z).$$

Hence, by chain rule and product rule, we deduce that

$$\frac{\partial^2}{\partial x_i \partial x_j} H_0^{(1)}(k|x-y|) = k^2 H_2^{(1)}(k|x-y|) \frac{(x-y)_i (x-y)_j}{|x-y|^2} - k \frac{1}{|x-y|} H_1^{(1)}(k|x-y|) \delta_{i,j},$$

where $\delta_{i,j}$ is the Kronecker delta function. Consequently, the fundamental solution $\Phi(x, y)$ is given by

$$\Phi(x, y)_{i,j} = \frac{ik^2}{4} \left[\left(H_0^{(1)}(k|x-y|) - \frac{H_1^{(1)}(k|x-y|)}{k|x-y|} \right) \delta_{i,j} + H_2^{(1)}(k|x-y|) \frac{(x-y)_i (x-y)_j}{|x-y|^2} \right].$$

Upon noting the recursive relation $\frac{2H_1^{(1)}(z)}{z} = H_0^{(1)}(z) + H_2^{(1)}(z)$ for Hankel functions [1], we deduce that the trace of the fundamental solution satisfies

$$\begin{aligned} \text{tr}(\Phi(x, y)) &= \frac{ik^2}{4} \left[2H_0^{(1)}(k|x-y|) - 2\frac{H_1^{(1)}(k|x-y|)}{k|x-y|} + H_2^{(1)}(k|x-y|) \right] \\ &= \frac{ik^2}{4} H_0^{(1)}(k|x-y|) = k^2 G(x, y). \end{aligned}$$

Next we turn to the three-dimensional case, i.e., $G(x, y) = \frac{1}{4\pi} \frac{e^{ik|x-y|}}{|x-y|}$. A direct calculation yields

$$\begin{aligned} \Phi(x, y)_{i,j} &= G(k|x-y|) \left[k^2 \left(\delta_{i,j} - \frac{(x-y)_i (x-y)_j}{|x-y|^2} \right) - \left(\delta_{i,j} - \frac{3(x-y)_i (x-y)_j}{|x-y|^2} \right) \frac{1}{|x-y|^2} \right. \\ &\quad \left. + ik \left(\delta_{i,j} - \frac{3(x-y)_i (x-y)_j}{|x-y|^2} \right) \frac{1}{|x-y|} \right]. \end{aligned}$$

Consequently, $\text{tr}(\Phi(x, y)) = 2k^2 G(x, y)$. \square

It follows from (17) that the sum of the diagonal components of the fundamental solution $\Phi(x, y)$ to the Maxwell system behaves like the scalar fundamental solution $G(x, y)$, which, according to the experimental evidences in [21], can provide an excellent probing function of the scatterer support. To be more precise, this yields

$$k^{-1} \Im(\text{tr} \Phi(x, y)) = \begin{cases} \frac{k^2}{4} \frac{J_0(k|x-y|)}{k}, & d = 2, \\ 2k^2 \frac{\sin(k|x-y|)}{k|x-y|}, & d = 3. \end{cases} \quad (18)$$

Therefore, the crucial quantity $k^{-1} \Im(\text{tr} \Phi(x_p, x_q))$ attains its maximum at $x_p = x_q$, indicating the presence of the scatterers. We note that apart from the global maximum, there are also a number of local maxima, which introduce ‘ripples’ into the resulting index. However, we note that the positions of the local maxima depend only on the known wavenumber k , and can be strictly calibrated.

Next, we examine combinations of the components of the fundamental solution $\Phi(x, y)$. We first note that each independent component $\Im \Phi_{ij}(x, x_q)$ does have a significant maximum at $x = x_q$ like (18). However, the magnitude of each component differs dramatically. In Fig. 1, we show the inner products of the components Φ_{11} , Φ_{22} , Φ_{12} with themselves (termed cross product for short) and the diagonal sum as a function of the sampling point $x_p \in \tilde{\Omega}$, i.e., $|\langle \Phi_{11}(x_p, x), \Phi_{11}(x_q, x) \rangle_{L^2(\Gamma)}|$ etc. We note that these cross products form the building blocks of the index function $\Psi(x_p; q)$, and their behaviors completely determine the performance of the DSM. The cross products for Φ_{11} and Φ_{22} exhibit significant directional resonance effects but their sum, i.e., $\langle \Phi_{11}(x, x_q), \Phi_{11}(x, x_p) \rangle_{L^2(\Gamma)} + \langle \Phi_{22}(x, x_q), \Phi_{22}(x, x_p) \rangle_{L^2(\Gamma)}$ does only assume one significant maximum at $x_q = x_p$ without much resonance effects. In practice, due to the mixing of these different components in the index $\Psi(x_p; q)$, the performance of the DSM may not be as good as that for the scalar Helmholtz case in the case of the scattered electric field E^s of one polarization p . Nonetheless, with multiple polarizations p_k and all components of the respective scattered field E^s , one might be able to approximate the trace $\text{tr} \Phi(x, y)$, and (18) can be applied. If this is indeed the case, then the performance of the sampling method would equal that for the scalar case.

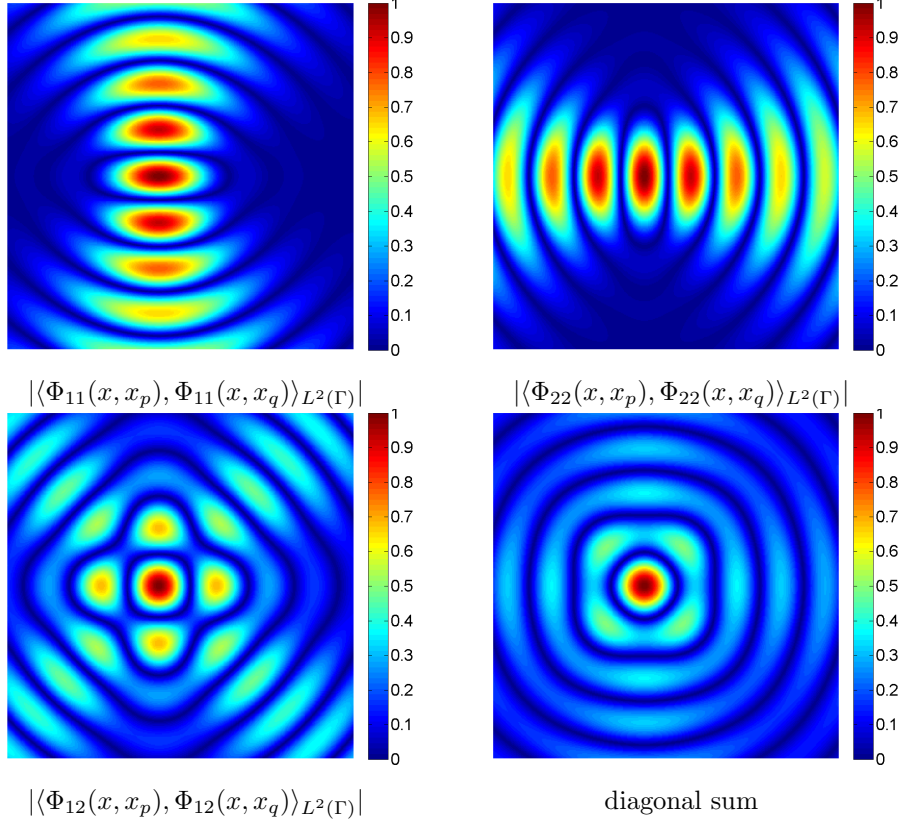


Figure 1: Cross products of Φ_{11} , Φ_{22} , Φ_{12} , with the point scatterer located at the $x_q = (-\frac{1}{4}, 0)$, and the diagonal sum, over the sampling domain $\tilde{\Omega} = [-2, 2]^2$. The quantities are normalized.

Index function for multiple incident fields. To arrive at an applicable effective index function for multiple incidents, we examine the behavior of the two-dimensional fundamental solution $\Phi(x, y)$ more closely. We first consider the incident direction $d_1 = \frac{\sqrt{2}}{2}(1, 1)$ and the polarization $p_1 = \frac{\sqrt{2}}{2}(1, -1)$, and assume that the local induced electrical current J is proportional to the polarized incident wave E^i within the inhomogeneity located at x_q . Upon ignoring the normalization, the index function $\Psi(x_p; q)$ with the choice $q = p_1$ is roughly determined by

$$\begin{aligned} \langle \Phi(x, x_q)p_1, \Phi(x, x_p)p_1 \rangle_{L^2(\Gamma)} &= \langle \Phi_{11}(x, x_q) - \Phi_{12}(x, x_q), \Phi_{11}(x, x_p) - \Phi_{12}(x, x_p) \rangle_{L^2(\Gamma)} \\ &\quad + \langle \Phi_{12}(x, x_q) - \Phi_{22}(x, x_q), \Phi_{12}(x, x_p) - \Phi_{22}(x, x_p) \rangle_{L^2(\Gamma)}, \end{aligned}$$

where each term in the inner products, like $\Phi_{11}(x, x_p) - \Phi_{12}(x, x_p)$ and so on, corresponds to one component of the vector field E^s . Similarly, for the incident direction $d_2 = \frac{\sqrt{2}}{2}(1, -1)$ and the polarization $p_2 = \frac{\sqrt{2}}{2}(1, 1)$, the index function $\Phi(x_p; q)$ with the choice $q = p_2$ is roughly determined by

$$\begin{aligned} \langle \Phi(x, x_q)p_2, \Phi(x, x_p)p_2 \rangle_{L^2(\Gamma)} &= \langle \Phi_{11}(x, x_q) + \Phi_{12}(x, x_q), \Phi_{11}(x, x_p) + \Phi_{12}(x, x_p) \rangle_{L^2(\Gamma)} \\ &\quad + \langle \Phi_{12}(x, x_q) + \Phi_{22}(x, x_q), \Phi_{12}(x, x_p) + \Phi_{22}(x, x_p) \rangle_{L^2(\Gamma)}. \end{aligned}$$

The quantities $|\langle \Phi(x, x_q)p_1, \Phi(x, x_p)p_1 \rangle_{L^2(\Gamma)}|$ and $|\langle \Phi(x, x_q)p_2, \Phi(x, x_p)p_2 \rangle_{L^2(\Gamma)}|$ after normalization are shown in Fig. 2: they exhibit strong resonances. This is attributed to the ripples predicted from the relation (18) and mixing of different components of the fundamental solution Φ . Note that the resonances show up at different regions, with their locations depending on the incident direction/polarization. We reiterate that in case of one single point scatterer, the resonance is completely predictable and one

might be able to remove them from the reconstructed images with suitable postprocessing. However, in the presence of multiple scatterers, the discrimination of the resonances from the true scatterers can be highly nontrivial. Therefore, it is highly desirable to design a sampling method that is free from significant resonances ab initio, by suitably adapting the choice of q in the probing function $\Phi(x, x_p)q$ and combining the indices for multiple polarizations. Let us consider the two polarizations $p_1 = \frac{\sqrt{2}}{2}(1, -1)$ and $p_2 = \frac{\sqrt{2}}{2}(1, 1)$, and measure all components of the scattered electric field E^s , in the hope of focusing on the genuine inhomogeneities. Then the performance of the combined index with $p_1 = \frac{\sqrt{2}}{2}(1, -1)$ and $p_2 = \frac{\sqrt{2}}{2}(1, 1)$ is approximately given by

$$\begin{aligned} & \langle \Phi(x, x_q)p_1, \Phi(x, x_p)p_1 \rangle_{L^2(\Gamma)} + \langle \Phi(x, x_q)p_2, \Phi(x, x_p)p_2 \rangle_{L^2(\Gamma)} \\ &= \langle \Phi_{11}(x, x_q), \Phi_{11}(x, x_p) \rangle_{L^2(\Gamma)} + 2\langle \Phi_{12}(x, x_q), \Phi_{12}(x, x_p) \rangle_{L^2(\Gamma)} + \langle \Phi_{22}(x, x_q), \Phi_{22}(x, x_p) \rangle_{L^2(\Gamma)}. \end{aligned}$$

Even though the indices for the polarizations p_1 and p_2 separately both have their own shadows of the point scatterer at $x_q = (-\frac{1}{4}, 0)$ (see Fig. 2(a)-(b)), the combination can isolate the point scatterer very well (see Fig. 2(c)). Hence, the combination of multiple polarizations can remedy the undesirable rippling phenomena. This suggests us the following combined index $\Psi_c(x_p)$ for the multiple polarizations $\{p_l\}_{l=1}^L$:

$$\Psi_c(x_p) = \frac{1}{L} \sum_{l=1}^L \Psi(x_p; p_l)$$

where $\Psi(x_p; p_l)$ refers to the index function for the polarization p_l (hence the l th incident field).

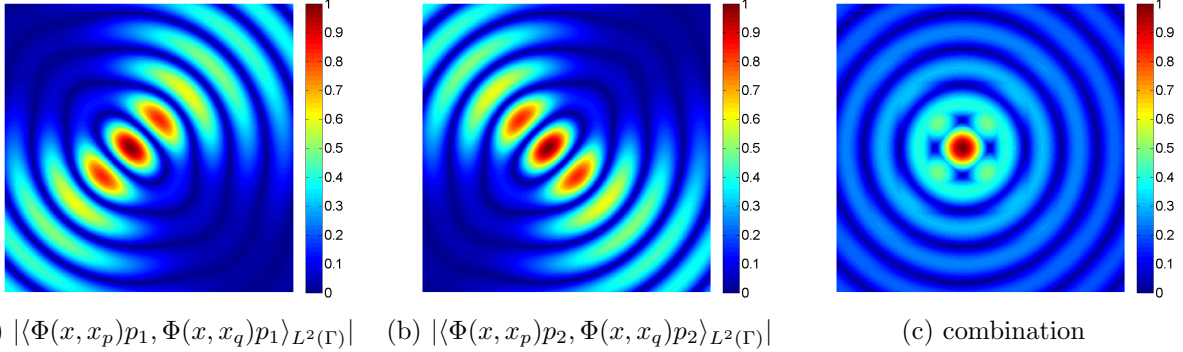


Figure 2: The cross products for polarizations p_1 , p_2 and the combination with direct sum over the sampling domain $\tilde{\Omega} = [-2, 2]^2$. The point scatterer is located at $x_q = (-\frac{1}{4}, 0)$. The quantities are normalized.

4 Numerical experiments and discussions

In this section, we present two- and three-dimensional numerical examples to showcase the features, e.g., the accuracy and robustness, of the proposed DSM for detecting scatterers. The examples are designed to illustrate the features of the method and to validate the theoretical findings in Section 3. Numerical results for both exact and noisy data will be presented. In all examples, the wavelength λ is set to 1, and the wavenumber k is 2π . The noisy scattered electric data E_δ^s is generated pointwise by

$$E_\delta^s(x) = E^s(x) + \varepsilon \max_{x \in \Gamma} |E^s(x)| \zeta(x),$$

where ε denotes the relative noise level, and both real and imaginary parts of the random variable $\zeta(x)$ follow the standard Gaussian distribution with zero mean and unit variance. All the computations were performed on a dual-core laptop using MATLAB R2009a.

4.1 Two-dimensional examples

Now we present numerical results for two-dimensional examples. Unless otherwise specified, two incident fields, i.e., $d_1 = \frac{\sqrt{2}}{2}(1, 1)^t$ and $d_2 = \frac{\sqrt{2}}{2}(-1, 1)^t$ (accordingly, the polarizations $p_1 = \frac{\sqrt{2}}{2}(1, -1)^t$ and $p_2 = \frac{\sqrt{2}}{2}(1, 1)^t$), are employed. For each incident field E^i , the scattered electric field E^s is measured at 30 points uniformly distributed on a circle of radius 5 centered at the origin. The sampling domain $\tilde{\Omega}$ is fixed at $[-2, 2]^2$, which is divided into small squares of equal side length $h = 0.01$. The index function Ψ as an estimate to the scatterer support will be displayed for each example.

Our first example shows the method for one single scatterer, which confirms the theoretical analysis of the index Ψ_c in Section 3.2.

Example 1. *The example considers one square scatterer of side length 0.3 centered at the point $(-\frac{1}{4}, 0)$. The true inhomogeneity coefficient $\eta(x)$ of the scatterer is set to be 1, namely $n(x) = \sqrt{2}$.*

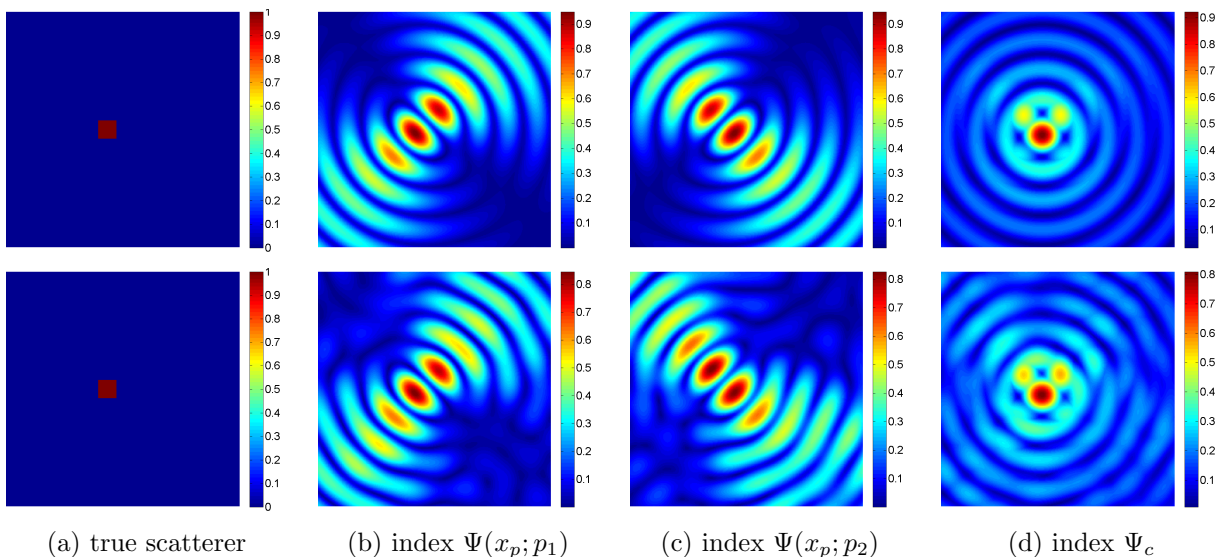


Figure 3: Numerical results for Example 1. The first and second row refers to index functions for the exact data and the noisy data with $\varepsilon = 20\%$ noise.

The numerical results for Example 1 are shown in Fig. 3. We observe that for sampling points close to the physical scatterer, the index function Ψ is relatively large; otherwise it takes relatively small values. Note that the image for one incident field E^i exhibits obvious resonances, with resonance locations depending on the incident direction. Here, the resonance behavior agree excellently with the theoretical analysis for one single point scatterer in Section 3.2, hence it might be removed by applying a suitable postprocessing procedure. Nonetheless, the use of two incident fields can greatly mitigate the resonances. Therefore, the index function Ψ_c does provide an accurate and reliable indicator for the location of the scatterer; see Fig. 3(d). The presence of $\varepsilon = 20\%$ noise in the measured data does not affect the shape of the index function Ψ_c , thereby showing the robustness of the method with respect to noise.

Our second example illustrates the method for two separate scatterers.

Example 2. *We consider two square scatterers, with the inhomogeneity coefficient η being 1 in both scatterers. The following two cases are investigated:*

- (a) *The two scatterers are of side length 0.2, and located at $(-0.8, -0.7)$ and $(0.3, 0.8)$, respectively.*
- (b) *The two scatterers are of side length 0.3, and located at $(-0.45, -0.35)$ and $(0.05, 0.15)$, respectively.*

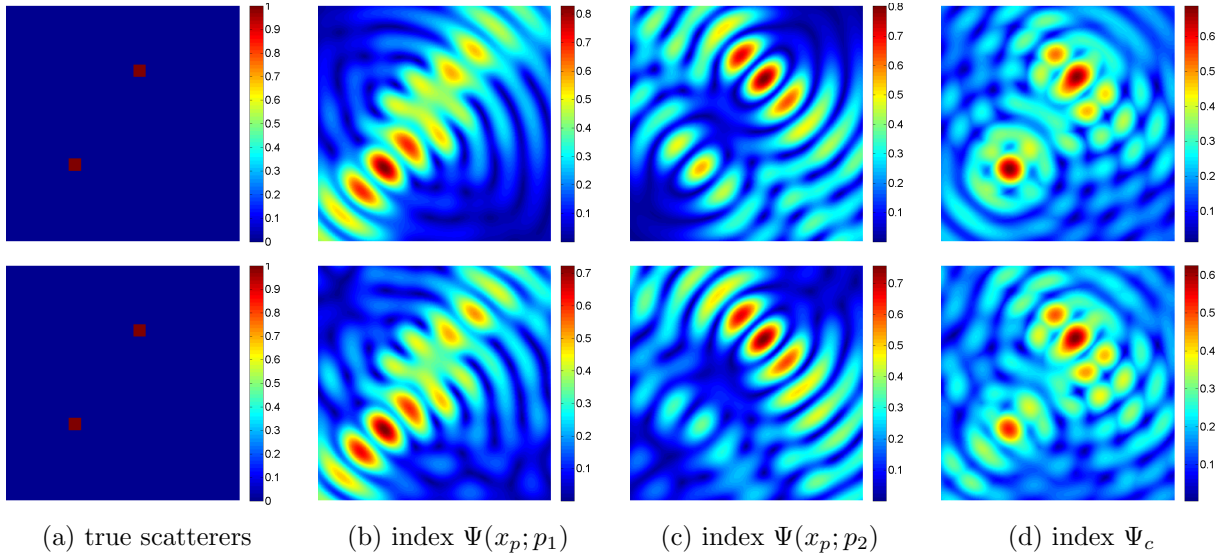


Figure 4: Numerical results for Example 2(a). The first and second row refer to index functions for the exact data and the noisy data with $\epsilon = 20\%$ noise.

The two scatterers in Example 2(a) are well apart from each other. In this example, each of the two incident fields tends to highlight only one of the two scatterers, with the index value for one scatterer being much higher than for the other; see Figs. 4(b)-(c). Since the two scatterers are well apart, the interactions between them is somehow weak, and the resonance pattern for the point scatterer is well kept. However, the two incident fields together give a clear discrimination of the two scatterers, with their locations satisfactorily recovered for both exact data and the data with $\epsilon = 20\%$ noise; see Fig. 4(d).

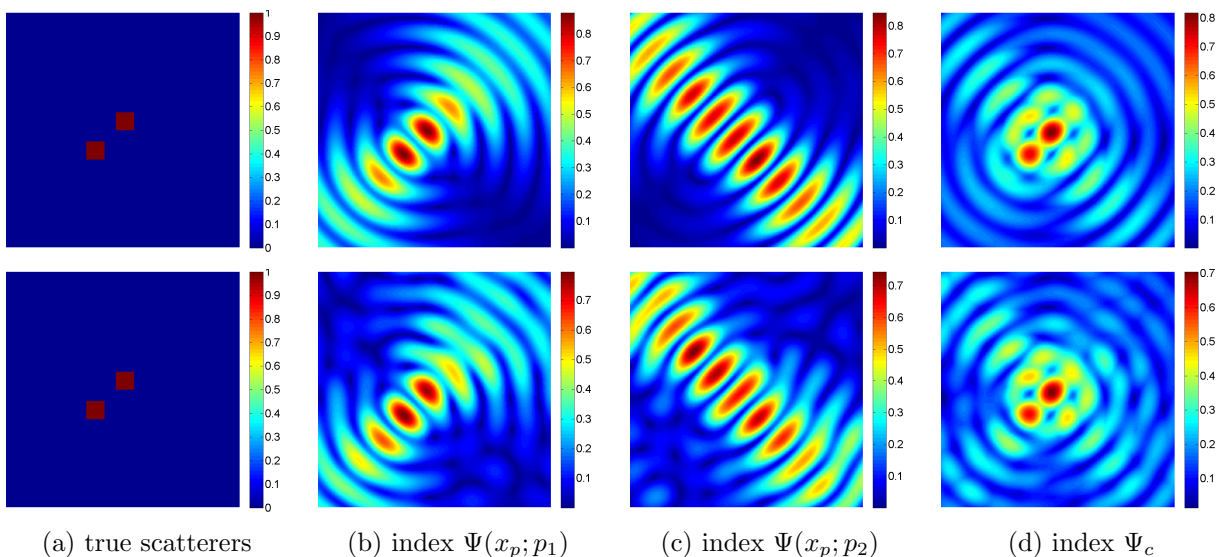


Figure 5: Numerical results for Example 2(b). The first and second row refer to index functions for the exact data and the noisy data with $\epsilon = 20\%$ noise.

The two scatterers in Example 2(b) stay very close to each other. We observe that, for the incident direction d_2 , apart from the strong resonances, the locations for the scatterers cannot be directly inferred since the index function Ψ relates the two scatterers into an elongated ellipse shape. Nonetheless, the

resonances were almost completely removed from the estimate when using two incident fields. Consequently, the estimate of the locations of the scatterers is very impressive: the two scatterers are still well separated despite their closeness, with their locations correctly estimated, for up to $\epsilon = 20\%$ noise in the data. Although not presented, we would like to remark that in the case of very high noise levels, e.g., $\epsilon = 40\%$, the estimate tends to connect the two scatterers, and also some spurious modes have emerged.

Our next example considers the more challenging case of three neighboring scatterers.

Example 3. *This example consists of three neighboring square scatterers of width 0.15: one located at $(-\frac{5}{8}, -\frac{5}{8})$, one located at $(-\frac{17}{40}, -\frac{17}{40})$, and one located at $(-\frac{21}{40}, \frac{1}{8})$. The inhomogeneity coefficients of all three scatterers are set to be $\eta = 1$.*

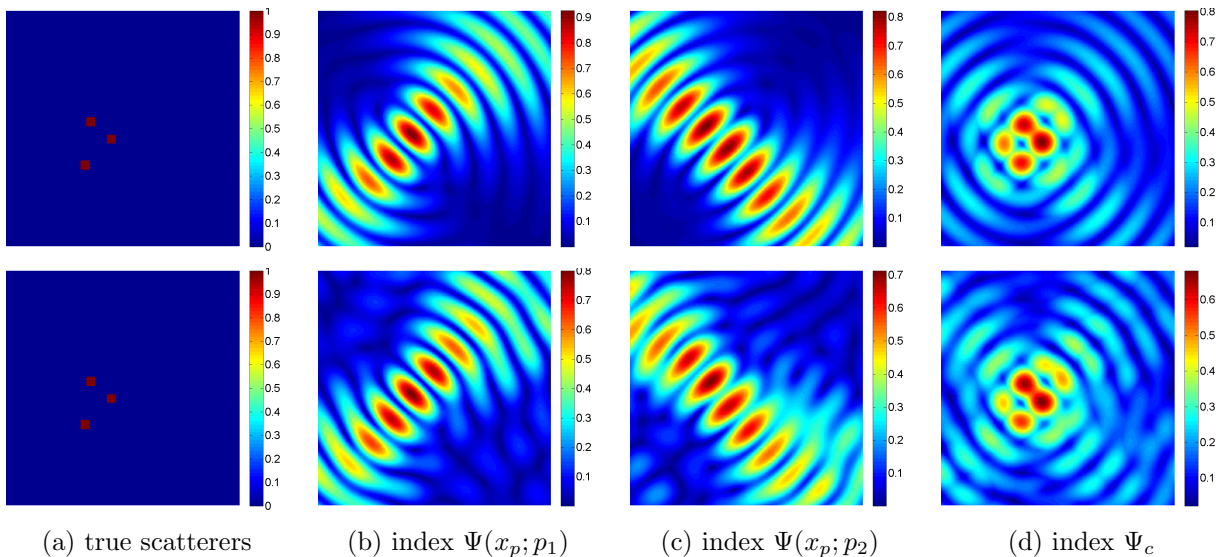


Figure 6: Numerical results for Example 3. The first and second row refer to index functions for the exact data and the noisy data with $\epsilon = 20\%$ noise.

In this example, the three scatterers stay very close to each other, especially the upper two, thus it is numerically very challenging to separate them. This is also reflected in the fact that each individual incident field tends to combine two of the three scatterers into one larger chunk, which is true for both the exact data and noisy data; see Figs. 6 (b)-(c). Therefore, it is difficult to tell from either Fig. 6(b) or Fig. 6(c) the number and locations of the scatterers. The latter is effectively remedied by using two incident fields together; see Fig. 6, where the three scatterers are vividly separated from each other. However, the interactions between the scatterers focus the strength on the scatterer to the right, and diminish slightly the strength of the scatterer to the left.

Next we consider a ring-shaped scatterer.

Example 4. *This scatterer is one ring-shaped square scatterer located at the origin, with the outer and inner side lengths being 0.6 and 0.4, respectively. The coefficient η of the scatterer is 1.*

The ring-shaped scatterer represents one of the most challenging objects to resolve, and it is highly nontrivial even with multiple data sets. The results with the exact data and $\epsilon = 20\%$ noise in the data are shown in Fig. 7. It is observed that with just two incident waves, the method can provide a quite reasonable estimate of the ring shape, and it remains very stable for up to $\epsilon = 20\%$ noise in the data.

4.2 Three-dimensional example

The last example shows the feasibility of the method for three-dimensional problems.

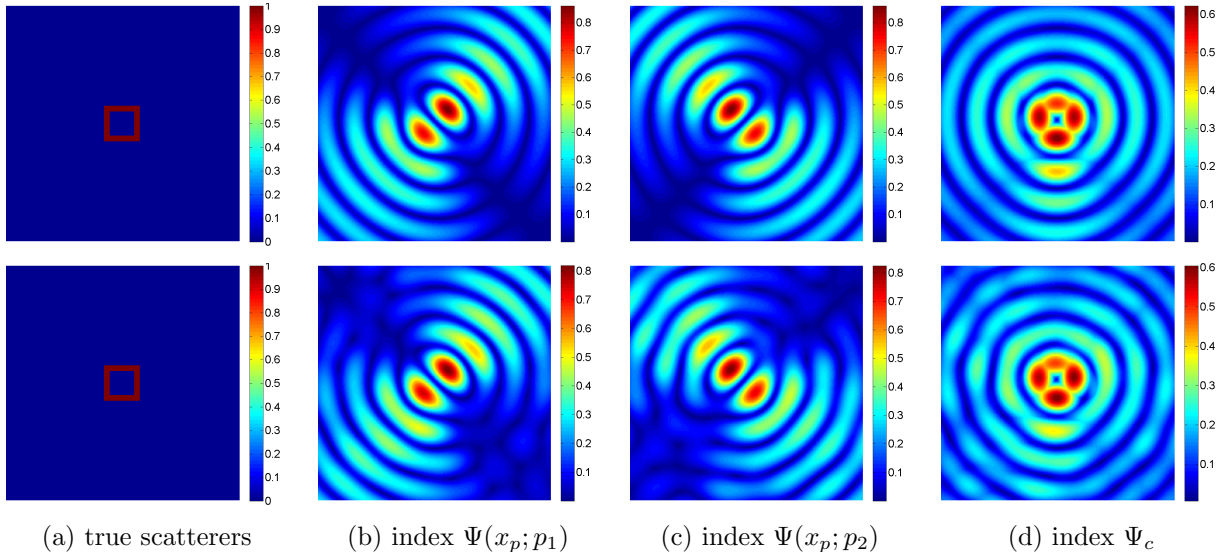


Figure 7: Numerical results for Example 4. The first and second row refers to index functions for the exact data and the noisy data with $\epsilon = 20\%$ noise.

Example 5. We consider two cubic scatterers with side length 0.2: one centered at $(0.4, 0.3, 0.3)$ and the other at $(-0.4, 0.3, 0.3)$, respectively, and the coefficient η in both scatterers is taken to be 1.

For this example, we take two incident fields, with the incident directions $d_1 = d_2 = \frac{1}{\sqrt{3}}(1, 1, 1)^t$ and the polarization vectors $p_1 = \frac{1}{\sqrt{6}}(1, -2, 1)^t$ and $p_2 = \frac{1}{\sqrt{6}}(1, 1, -2)^t$. The scattered field E^s is measured at the points on a uniformly distributed mesh of 10×10 on each face of the cube of edge length 10. The sampling domain $\tilde{\Omega}$ for evaluating the index functions is taken to be $[-2, 2]^3$. The problem is discretized with a mesh size 0.02. The numerical results are shown in Fig. 8. We observe that the support estimated by the index Ψ agrees very well with the exact one, the magnitude of the index Ψ decreases quickly away from the boundary of the true scatterers. The presence of $\epsilon = 20\%$ data noise (cf. Fig. 9), seems to cause no obvious deterioration of the accuracy of the index Ψ as compared with the exact data. By examining the cross-sectional images of the index, we found that in comparison with the two-dimensional problems, the rippling phenomenon seems less pronounced for this three-dimensional example.

5 Conclusions

We have developed a novel direct sampling method for the inverse electromagnetic medium scattering problem of estimating the support of inhomogeneities from scattered electric near-field data. It was derived based on an integral representation of the scattered field via the fundamental solution, a careful analysis on electromagnetic scattering and the behavior of the fundamental solutions. The method is particularly attractive in that it is applicable to a few incident fields. Methodologically, it involves only computing inner products of the scattered electric field with fundamental solutions located at the sampling points, hence it is strictly direct, straightforward to implement, computationally very efficient, and very robust with respect to the presence of data noise. The experimental results for two- and three-dimensional examples indicate that it can provide, after thresholding with a suitable cutoff value, a quite satisfactory estimate of the shapes of the scatterers from the measured data corresponding to only one or two incident directions, even in the presence of a large amount of noise.

In the present study, we have focused only on the very cheap direct sampling method for the reconstructions of the scatterers. It is natural to enhance the reconstructions by other more expensive but more accurate methods. More specifically, one can use the reconstructions by the direct sampling

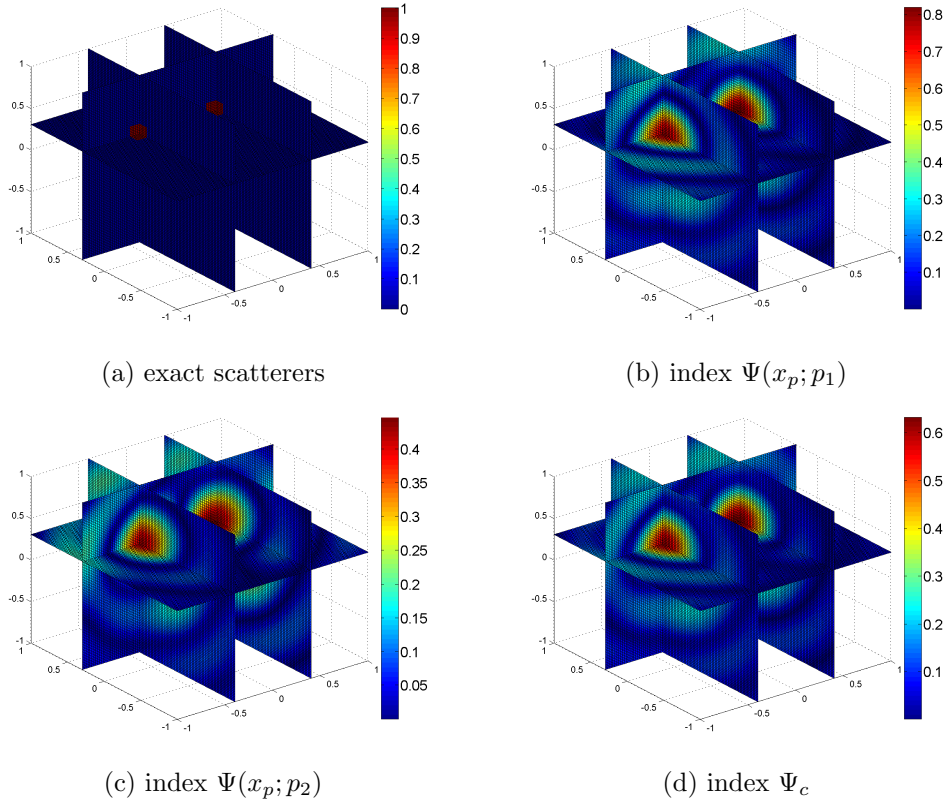


Figure 8: Numerical results for Example 5 with exact data.

method as the initial computational domain for those more refined methods to retrieve more accurate shapes of the scatterers and their physical medium properties, e.g., Tikhonov regularization [20]. Since the indirect imaging methods often involve highly nonlinear optimization processes, a more accurate and much smaller initial domain can essentially reduce the relevant computational costs.

It is also interesting to see the extensions of the direct sampling method for other important scattering scenarios, e.g., scattering from lines (cracks), far-field measurements and multiple-frequency data, as well as their theoretical justifications.

Acknowledgements

The work of BJ was supported by award KUS-C1-016-04, made by King Abdullah University of Science and Technology (KAUST), and that of JZ was substantially supported by Hong Kong RGC grants (projects 405110 and 404611).

A Numerical method for forward scattering

In this part we describe our numerical method for the integral equation (5) for two-dimensional domains Ω . We denote by \mathbb{J} the index set of grid points $x_j = (x_{j_1}^1, x_{j_2}^2)$, $j = (j_1, j_2) \in \mathbb{J}$, of a uniformly distributed mesh with a mesh size $h > 0$ and the square cells B_j given by

$$B_j = B_{j_1, j_2} = (x_{j_1}^1, x_{j_2}^2) + [-\frac{h}{2}, \frac{h}{2}] \times [-\frac{h}{2}, \frac{h}{2}]$$

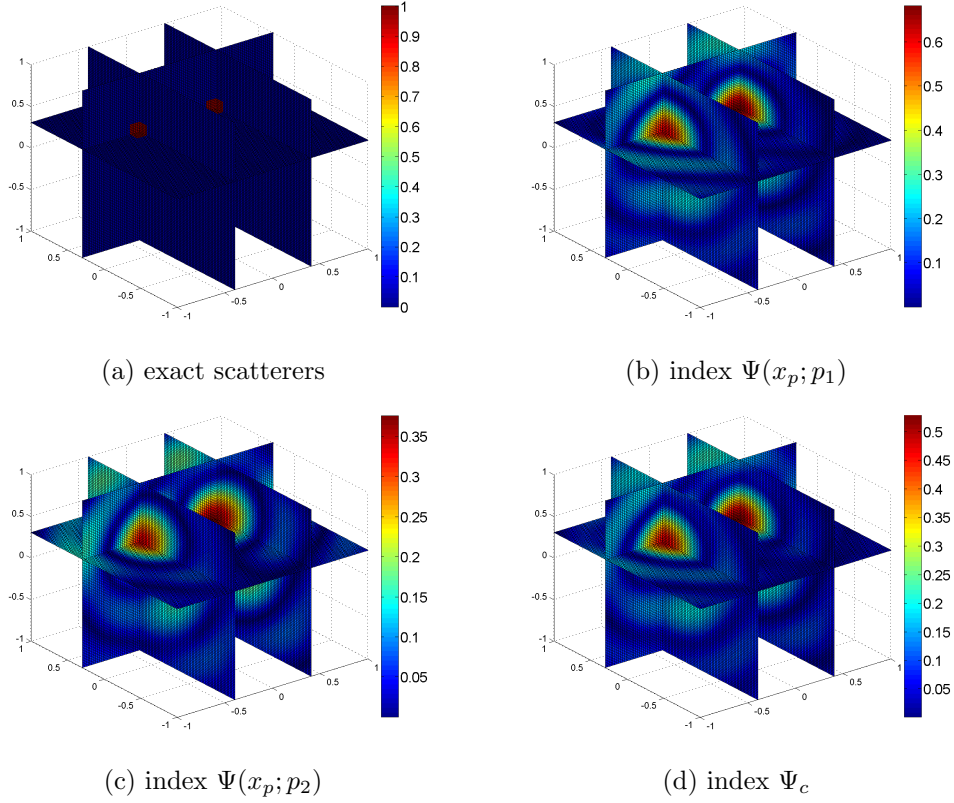


Figure 9: Numerical results for Example 5 with $\epsilon = 20\%$ data noise.

for every tuple $j = (j_1, j_2)$ in the index set \mathbb{J} . Further, we assume that the set $\cup_{j \in \mathbb{J}} B_j$ contains the scatterer support Ω . We shall approximate the integral operator in (5) by the mid-point quadrature rule, i.e.,

$$J_k + \eta_k \sum_{j \in \mathbb{I}} G_{k,j} (PJ)_j h^2 = \eta_k E^i(x_k) \quad (19)$$

where $J_k = J(x_k)$ and $\eta_k = \eta(x_k)$, and the off-diagonal entries $G_{k,j}$ and the diagonal entries $G_{k,k}$ are given by $G_{k,j} = G(x_k, x_j)$ and

$$G_{k,k} = \frac{1}{h^2} \int_{(-\frac{h}{2}, \frac{h}{2})^2} G(x, 0) dx,$$

respectively. The diagonal entries $G_{k,k}$ can be accurately computed by a tensor-product Gaussian quadrature rule. To arrive at a fully discrete scheme, we further approximate the crucial term PJ in equation (19) by the central finite difference scheme:

$$PJ = k^2 \begin{pmatrix} J & \\ & J \end{pmatrix} + \begin{pmatrix} D_{x_1 x_1} & D_{x_1 x_2} \\ D_{x_1 x_2} & D_{x_2 x_2} \end{pmatrix} J,$$

where $D_{x_i x_j}$ refers to taking the second-order derivative with respect to x_i and x_j . In practice, we shall approximate $D_{x_i x_j}$ by central finite difference scheme, i.e.,

$$D_{x_1 x_1} = H \otimes I, \quad D_{x_2 x_2} = I \otimes H, \quad D_{x_1 x_2} = D \otimes D,$$

where \otimes is the Kronecker product for matrices, H and D are the tridiagonal matrices for the second derivative and the first derivative, respectively. The resulting system can be solved using standard

numerical solvers, e.g., Gaussian elimination, if the cardinality of the index set \mathbb{J} is medium, or iterative solvers like generalized minimal residual method (GMRES) [27] should be applied if the cardinality of \mathbb{J} is large. Clearly, the extension of the procedure to 3D problems is straightforward. Our numerical experiences indicate that tens of GMRES iterations already yield a very accurate solution to the linear system.

References

- [1] M. Abramowitz and I. A. Stegun. *Handbook of Mathematical Functions with Formulas, Graphs, and Mathematical Tables*. Govt. Print. Off., Washington, 1968.
- [2] A. Abubakar, T. M. Habashy, P. M. van den Berg, and D. Gisolf. The diagonalized contrast source approach: an inversion method beyond the Born approximation. *Inverse Problems*, 21(2):685–702, 2005.
- [3] H. Ammari, E. Iakovleva, D. Lesselier, and G. Perrusson. MUSIC-type electromagnetic imaging of a collection of small three-dimensional inclusions. *SIAM J. Sci. Comput.*, 29(2):674–709, 2007.
- [4] G. Bao and P. Li. Inverse medium scattering problems for electromagnetic waves. *SIAM J. Appl. Math.*, 65(6):2049–2066, 2005.
- [5] G. Bao and P. Li. Numerical solution of an inverse medium scattering problem for Maxwell’s equations at fixed frequency. *J. Comput. Phys.*, 228(12):4638–4648, 2009.
- [6] A. E. Bulyshev, A. E. Souvorov, S. Y. Semenov, V. G. Posukh, and Y. E. Sizov. Three-dimensional vector microwave tomography: theory and computational experiments. *Inverse Problems*, 20(4):1239–1259, 2004.
- [7] F. Cakoni, D. Colton, and P. Monk. *The Linear Sampling Method in Inverse Electromagnetic Scattering*. SIAM, 2011.
- [8] X. Chen and Y. Zhong. MUSIC electromagnetic imaging with enhanced resolution for small inclusions. *Inverse Problems*, 25(1):015008, 12, 2009.
- [9] W. C. Chew and Y. M. Wang. An iterative solution of the two-dimensional electromagnetic inverse scattering problem. *Int. J. Imag. Sys. Tech.*, 1(1):100–108, 1989.
- [10] D. Colton and A. Kirsch. A simple method for solving inverse scattering problems in the resonance region. *Inverse Problems*, 12(4):383–393, 1996.
- [11] D. Colton and R. Kress. *Inverse Acoustic and Electromagnetic Scattering Theory*. Springer-Verlag, Berlin, 2 edition, 1998.
- [12] T. J. Cui, W. C. Chew, A. A. Aydinler, and S. Chen. Inverse scattering of two-dimensional dielectric objects buried in a lossy earth using the distorted Born iterative method. *IEEE Trans. Geosci. Rem. Sens.*, 39(2):339–346, 2001.
- [13] J. De Zaeytijd, A. Franchois, C. Eyraud, and J.-M. Geffrin. Full-wave three-dimensional microwave imaging with a regularized GaussNewton method - theory and experiment. *IEEE Trans. Antenn. Prop.*, 55(11):3279–3292, 2007.
- [14] A. J. Devaney. Super-resolution processing of multi-static data using time-reversal and music. available at http://www.ece.neu.edu/faculty/devaney/preprints/paper02n_00.pdf, 1999.
- [15] O. Dorn, H. Bertete-Aguirre, J. G. Berryman, and G. C. Papanicolaou. A nonlinear inversion method for 3D electromagnetic imaging using adjoint fields. *Inverse Problems*, 15(6):1523–1558, 1999.

- [16] O. Dorn and D. Lesselier. Level set methods for inverse scattering. *Inverse Problems*, 22(4):R67–R131, 2006.
- [17] T. M. Habashy, R. W. Groom, and B. R. Spies. Beyond the Born and Rytov approximations: a nonlinear approach to electromagnetic scattering. *J. Geophys. Res.*, 98(B2):1759–1775, 1993.
- [18] T. Hohage. Fast numerical solution of the electromagnetic medium scattering problem and applications to the inverse problem. *J. Comput. Phys.*, 214(1):224–238, 2006.
- [19] T. Hohage and S. Langer. Acceleration techniques for regularized Newton methods applied to electromagnetic inverse medium scattering problems. *Inverse Problems*, 26(7):074011, 15 pp., 2010.
- [20] K. Ito, B. Jin, and J. Zou. A two-stage method for inverse medium scattering. *J. Comput. Phys.*, 2012, in press. available at <http://arxiv.org/abs/1205.4277>.
- [21] K. Ito, B. Jin, and J. Zou. A direct sampling method to inverse medium scattering problem. *Inverse Problems*, 28(2):025003, 11 pp., 2012.
- [22] A. Lakhali. A decoupling-based imaging method for inverse medium scattering for Maxwell’s equations. *Inverse Problems*, 26(1):015007, 17, 2010.
- [23] A. Lakhali and A. K. Louis. Locating radiating sources for Maxwell’s equations using the approximate inverse. *Inverse Problems*, 24(4):045020, 18, 2008.
- [24] J. Li and J. Zou. A direct sampling method for inverse scattering using far-field data. *Inverse Problems and Imaging*, 2012, in press. Available at arXiv:1206.0727.
- [25] R. Potthast. A survey on sampling and probe methods for inverse problems. *Inverse Problems*, 22(2):R1–R47, 2006.
- [26] R. Potthast. A study on orthogonality sampling. *Inverse Problems*, 26(7):074015, 17 pp., 2010.
- [27] Y. Saad. *Iterative Methods for Sparse Linear Systems*. SIAM, Philadelphia, PA, second edition, 2003.
- [28] S. Y. Semenov, R. H. Svenson, A. E. Bulyshev, A. E. Souvorov, A. G. Nazarov, Y. E. Sizov, A. V. Pavlovsky, V. Y. Borisov, B. A. Voinov, G. I. Simonova, A. N. Starostin, V. G. Posukh, G. P. Tatsis, and V. Y. Baranov. Three-dimensional microwave tomography: experimental prototype of the system and vector Born reconstruction method. *IEEE Trans. Biomed. Eng.*, 46(8):937–946, 1999.
- [29] H. Tortel, C. Micolau, and M. Saillard. Decomposition of the time-reversal operator for electromagnetic scattering. *J. Electr. Waves Appl.*, 13:687–719, 1999.
- [30] M. Vögeler. Reconstruction of the three-dimensional refractive index in electromagnetic scattering by using a propagation-backpropagation method. *Inverse Problems*, 19(3):739–753, 2003.
- [31] C. Weber and P. Werner. Regularity theorems for Maxwell’s equations. *Math. Meth. Appl. Sci.*, 3(1):523–536, 1981.